



Structure and corrosion of Al-40 wt.% Nb-2 wt.% X alloys rapidly solidified from the melt

F. Layachi¹ · M. Y. Debili¹

Received: 8 October 2021 / Accepted: 10 April 2022 / Published online: 25 April 2022
© The Author(s), under exclusive licence to Springer Nature B.V. 2022

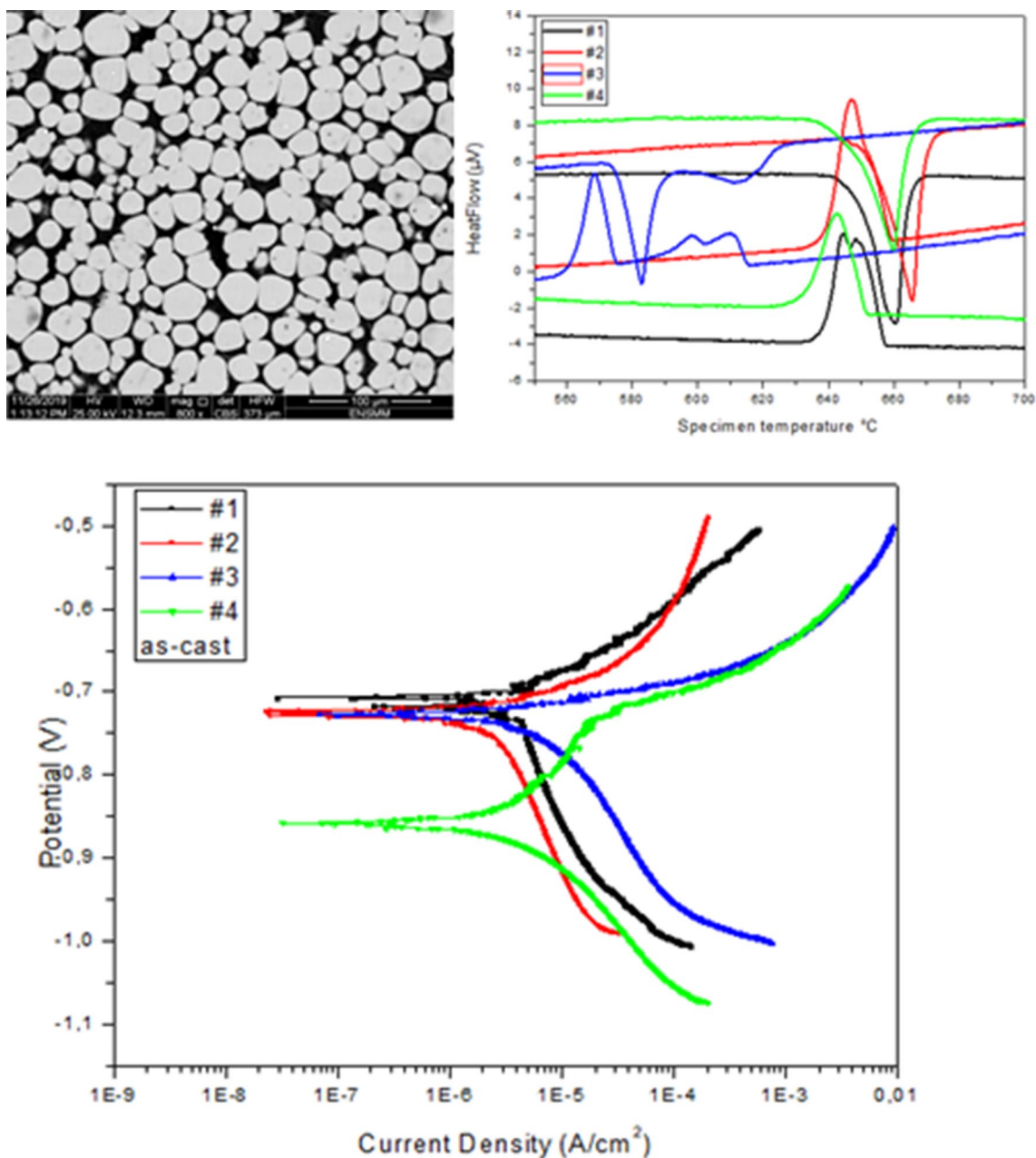
Abstract

The addition of a ternary element such as boron, silicon, or titanium to the binary alloy Al-40 wt.% Nb produced by rapid solidification after electromagnetic fusion results in a modification of the alloy behavior toward corrosion resistance in a saline medium (3.5 g/l NaCl), as measured by potentiodynamic polarization curves and electrochemical impedance spectroscopy (EIS) on both as-cast and annealed specimens. Optical microscopy, X-ray diffraction (XRD), and scanning electron microscopy (SEM) were used to characterize the binary Al-40 wt.% Nb alloy #4 and ternary Al-40 wt.% Nb-2 wt.% X (X: B alloy #1, Ti alloy #3, Si alloy #2) alloys, as well as EDS quantitative analysis combined with differential thermal calorimetry (DSC). Except for a smaller particle size in alloy #1 when compared to binary alloy #4, the as-cast solidification microstructure reveals no significant shape changes. When compared to other treated alloys, including binary alloys, heat-treated alloy #3 stands out electrochemically, and as-cast binary alloy # 4 also shines out when compared to cast ternary alloys, demonstrating that microstructure is essential.

✉ M. Y. Debili
mydebili@yahoo.fr

¹ Laboratory of Magnetism and Spectroscopy of Solids LM2S,
Department of Physics, Faculty of Science, Badji Mokhtar
Annaba University, BP. 12, 23000 Annaba, Algeria

Graphical Abstract



Keywords Aluminum · Niobium · Corrosion · Solidification · Structure · Ternary alloys

1 Introduction

Aluminum is more commonly utilized as an alloy in order to improve its mechanical and structural capabilities at high temperatures [1]. Aluminum alloys have the advantage of having a high mechanical strength while maintaining a low density [2], allowing them to be utilized in a variety of industries such as aeronautics, automotive, and architecture,

including roofs, facades, and interior design, decorating, and packaging [3–5]. By changing the stoichiometry and crystal structures of intermetallic alloys, new materials can be created very easily. Transition metal aluminides, such as AlFe, AlNi, and AlCo [6], have intriguing magnetic characteristics [6, 7]. They are corrosion and oxidation resistant. Al-Nb alloys are notable for their high strength, high melting point, low density, and good oxidation resistance

as sacrificial anodes by cathodic protection in seawater of steel [8]. Al-Nb alloys are additionally distinguished by Niobium's near-zero solubility in aluminum, as well as the creation of the intermetallic compound trialuminide Al_3Nb [9, 10]. Many applications require the characterization of solidification microstructures [11]. However, due to the complexity of most alloys' compositions, such an examination is challenging [12]. Rapid solidification (RS) [11] and physical vapor deposition (PVD) [13] are two processes for producing microcrystalline and nanocrystalline materials, and the final material has a polycrystalline structure with no orientation of the preferred crystallographic grain. Because of the creation of the protective layer of oxide Al_2O_3 , diluted aluminum alloys have strong corrosion resistance, which can be increased by anodization [14]. Most researchers [15, 16] acknowledge that preventing aluminum corrosion via pitting in a humid climate is a big difficulty. Aluminum alloys are susceptible to galvanic corrosion, thus caution should be exercised when working with iron and copper [8]. It should be highlighted that alloys in the 2000 and 7000 series have intergranular corrosion and stress corrosion risks [17]. Pitting corrosion is the most prevalent kind of aluminum corrosion in saltwater, and because the pH of seawater (8 to 8.5) is in the region where aluminum and its alloys are susceptible to this type of corrosion, the rate of pitting of aluminum tends to slow down over time. Aluminum is known to pit in Cl^- containing water, especially near fissures or stagnant zones where the passivity is disrupted by differential aeration cells [18, 19]. Aluminum pitting corrosion is a more harmful kind of corrosion. It shows as irregularly shaped holes on the metal's surface and sinks. The diameter and depth of the wells are determined by the type of material, corrosive medium, and environmental conditions that aluminum and its alloys are subjected to. Aluminum is a metal that reacts swiftly to oxidation thermodynamically, and it has strong corrosion resistance in practice. The appropriate choice of extra elements, on the other hand, reduces the risk of corrosion [20]. Element alloys are used to improve qualities that are difficult to get when working with a pure metal. Boron is added to primary aluminum grains to refine them [21–25], enhance corrosion resistance, and improve

mechanical performance [25–28]. A little quantity of boron added to cast pure titanium and $\text{Ti}_{0.5}\text{Si}$ alloy improves tensile strength and elongation [29]. Yen et al. [30] discuss the influence of boron additions on the microstructure and transverse properties of directionally solidified superalloys. When boron was introduced, the transverse creep lifetime and tensile characteristics significantly improved. The ternary Al-Nb-Si system is an outstanding superconducting material as well as a potential material for use in niobium silicide-based composites with great practical qualities comparable to nickel-based super alloys [31]. When compared to the as-cast condition, heat treatment of Al-Si alloy and its composites resulted in significant improvements in corrosion resistance [32]. The electrochemical behavior [33–36] and mechanical properties of Al matrix [34] are influenced by silicon content in the microstructure. Increased silicon concentration increases the tensile strength of aluminum alloys by up to 6% [37]. The increase in silicon content causes dendritic refinement and a more extensive redistribution of the eutectic mixture, resulting in a decrease in corrosion resistance [33]. Because of its low elastic modulus, high biocompatibility, specific strength, good formability, corrosion resistance, and specific strength, titanium (Ti) and its alloys are used in biomedical applications [38]. Increasing the Ti concentration in aluminum alloys to a level above the standard practice for grain refining can improve corrosion characteristics [39]. In equilibrium conditions, titanium is regarded as a low diffusivity alloying element in aluminum [40]. The current challenge is to generate and develop light alloys with superior mechanical and corrosion resistance to meet the rising demand for materials produced for applications that combine energy efficiency with a reduction in greenhouse gas emissions [41]. To that end, we hope to demonstrate in this paper how critical it is to develop the Al-40% Nb-20% M(M: B, Si, Ti) alloy system by rapid solidification after melting under electromagnetic induction, as well as the role that each element added separately to the Al-40% Nb alloy can play in refining the microstructure and improving corrosion and mechanical resistance.

Table 1 Weight percent targeted compositions of the alloys

Alloy	w% Al	w% Nb	wt.% B	wt.% Ti	wt.% Si
#1	60	40	2	–	–
#2	60	40	–	2	–
#3	60	40	–	–	2
#4	60	40	–	–	–

2 Experimental details

2.1 Preparation of the alloys

To assess the structural and electrochemical behavior, four alloys with different chemical compositions of the systems (Al, Nb), (Al, Nb, Ti), (Al, Nb, Si), and (Al, Nb, B) were produced by electromagnetic fusion under induction and rapidly solidified at room temperature. Commercial Al and Nb, Si, Ti, and B elemental powders (99.9% purity) were blended and cold compacted into a cylinder for the first time, and the density of the product was intended for high-frequency induction fusion (HF) and rapidly quenched. Linn Therm 600 type (300 kHz) apparatus has a primary vacuum and a power of 6 Kw. Each sample has a total mass of 5 g before it is prepared. Table 1 provides the target Al, Nb, B, Ti, and Si compositions for each alloy. The samples were then cut with a microtome before being mechanically polished with (600–4000) SiC grinding paper and etched using Keller's reagent solution of (5 ml HF + 9 ml HCl + 22 ml HNO₃ + 74 ml H₂O) for 10 s, after which the bulk was treated at 500 °C for 60 min and air-cooled.

2.2 Characterization techniques

DSC thermograms were obtained using a DSC type LAB-SYS EVO with alumina crucibles to heat the sample under an argon atmosphere. The samples were heated with a temperature rise rate of 12 °C/min in the temperature range of 30–800 °C. For electrochemical characterization, the surface was mechanically polished with SiC emery paper and subsequently treated to remove the impurities by two successive baths of acetone (99.5%) then ethanol (95%) and finally rinsed in deionized water. X-ray diffraction analysis

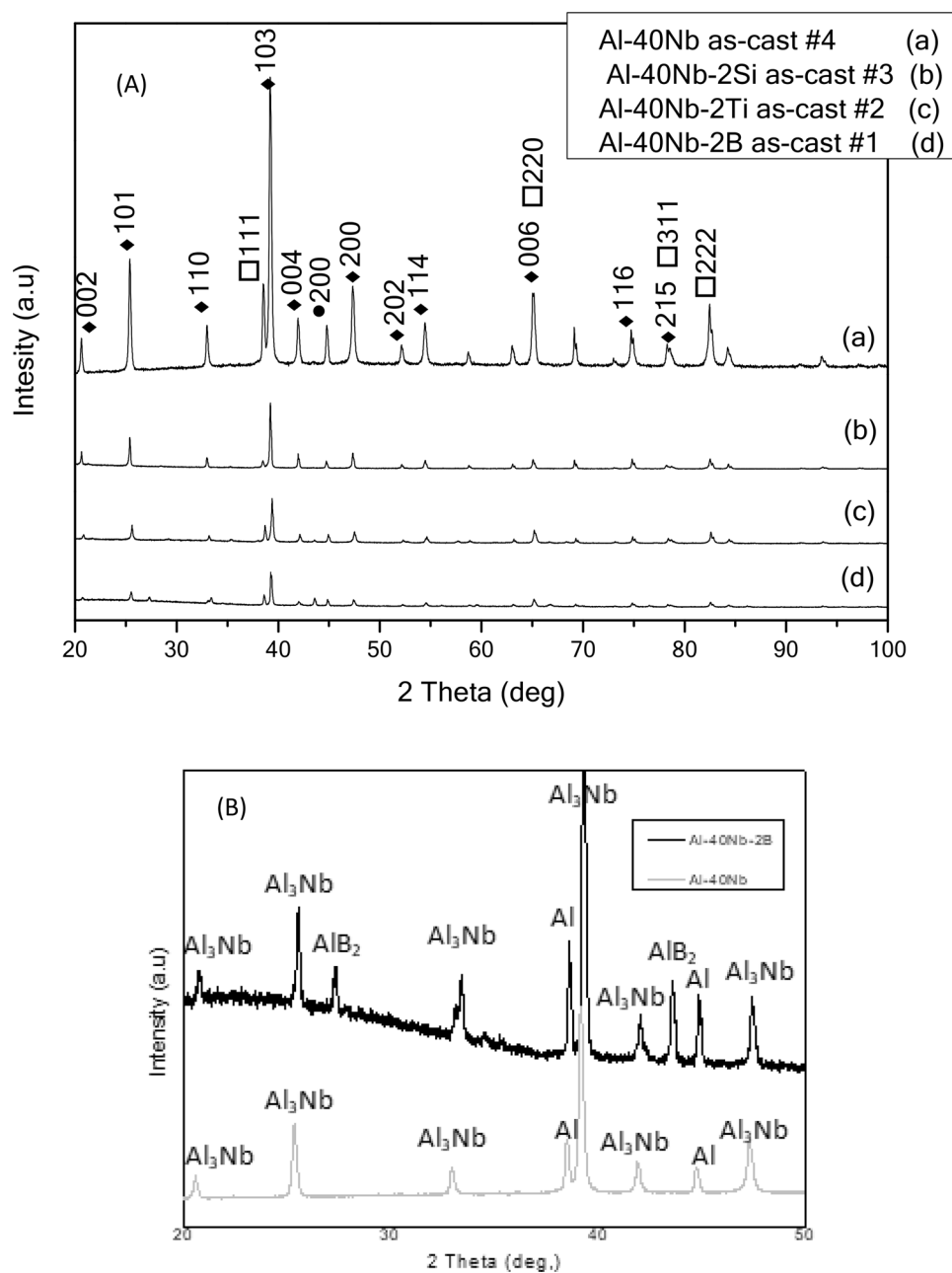
was accomplished with copper anticathode (1.54 Å) from 10° to 100° in 2θ. Electrochemical measurements were performed using a PARSTAT 4000 instrument, controlled by a microcomputer with Versa Studio software to record the curves of polarization, connected to a cell to three electrodes potentiostat manufactured. The electrochemical cell is mounting to three electrodes. The used electrodes are: the working electrode which is the sample, the reference in saturated calomel electrode (SEC) of KCl (E = 0,242 V), and the counter electrode was graphite rode. All the experiments were measured in a corrosive medium by using a solution of sodium chloride (NaCl) to 3.5% for 24 h under potential in open circuit (OCP). The potential that is our equilibrium potential was measured after 24 h. Then polarization curves were recorded with a sweep of an interval –250 mV at 250 mV, compared with the equilibrium potential, and a 0.5 mV/s scanning speed to record the curve of polarization. The electrochemical measurements were performed at room temperature. Electrochemical impedance spectroscopy (EIS) measurements were performed at an open circuit potential (OCP) in the frequency range from 0.1 Hz to 1000 kHz and amplitude equal to 10 (mV RMS). EC-Lab® V10.37 software was used to fit Nyquist plots curves to get a complex equivalent circuit. The surface morphologies of the samples before and after the corrosion test were investigated by light microscopy (Nikon ECLIPS LV150N) and scanning electron microscopy SEM FEI Quanta 250 apparatus equipped with electron dispersion spectroscopy (EDS).

3 Results and discussion

3.1 X-ray diffraction analysis

Figure 1a displays the diffraction patterns of the alloys. In binary alloy, apart from the diffraction peaks emanating from the FCC α-Al solid solution phase according to JCPDS cards 00–004-0787 [42], there are peaks from Al₃Nb tetragonal intermetallic compound according to JCPDS cards 00–004-0787 [42], this is in agreement with the phase diagram of the Al-Nb system [43]. The diffraction peak (111)Al located at 2θ = 38° is close to that of (103)Al₃Nb

Fig. 1 A. X-ray diffraction pattern of Al-Nb-X alloys (\square Al, \blacklozenge Al_3Nb). B. X-ray diffraction patterns of Al-40%Nb (alloy#4) as-cast and Al-40%Nb-2%B (alloy #1) as-cast showing peaks of AlB_2 phase



located at $2\theta = 39^\circ$, the latter is more intense than that of aluminum both in the binary alloy and in the three ternary alloys considered, which proves the relatively high amount of the Al_3Nb phase to the detriment of the α -Al phase. Furthermore, no other additional diffraction peak that may come from a possible intermetallic phase in which titanium or

silicon will be involved is detectable in any of the diffraction diagrams containing 2 wt.% of the addition, this is in favor of a supersaturated aluminum solid solution which can give rise to a solid solution hardening effect. On the other hand, for the alloy containing boron, we observe the presence of diffraction peaks due to the AlB_2 phase, Fig. 1b, according

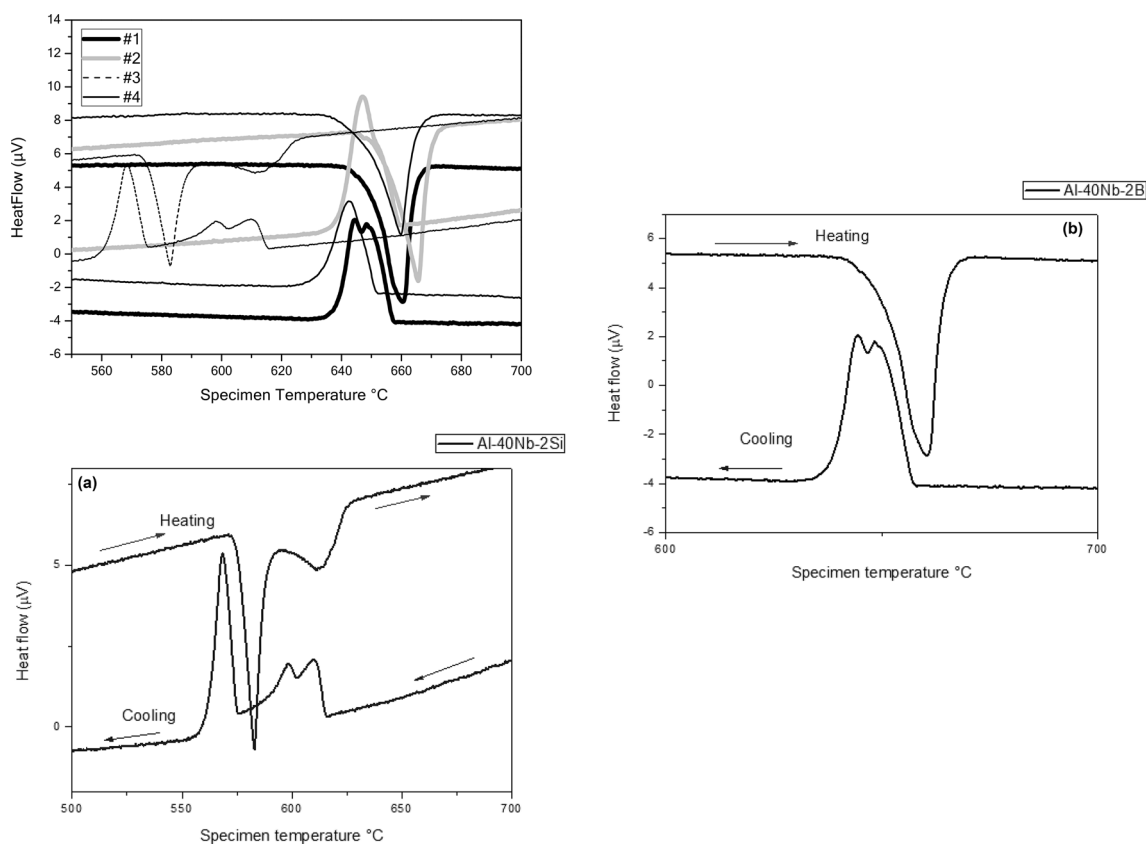


Fig. 2 Heating–cooling (partial temperature range) enlarged zone. **a.** Enlarged zone of the Al-40Nb-2Si thermogram. **b.** Enlarged zone of the Al-40Nb-2B thermogram

to JCPDS card 39–1483 with the space group P6/mmm and lattice parameters of $a = 0.3009$ nm and $c = 0.3262$ nm [44].

3.2 Thermal analysis by DSC

Figure 2 shows the superposition of the DSC thermograms recorded after a heating–cooling cycle at a rate of $12^\circ/\text{min}$, of the different alloys, comparatively to the binary Al-40 wt.% Nb. We note that except for the ternary Al-40 wt.% Nb-2 wt.% Si, all the alloys have an endothermic peak corresponding to the melting of aluminum at the narrow temperature range of $660\text{--}665^\circ\text{C}$ which is predictable for this kind of alloys based on aluminum

and by the literature [45]. The alloy Al-40% Nb-25% Si differs from the others in that it exhibits its first endothermic peak on heating, which most likely corresponds to aluminum melting, at a temperature higher than expected and which is around 610°C ; a second peak situated at 577°C may be attributed to the eutectic transformation, α Al-Si [46], Fig. 2a. Another striking fact in Fig. 2 is the shape of the exothermic peak on cooling in the Al-40% Nb-2% B alloy and which should probably correspond to that of the crystallization of aluminum, indeed this peak presents a clearly visible duplication, Fig. 2b. This could be likened to the crystallization of α Al solid solution and α Al-AlB₂ eutectic [47, 48].

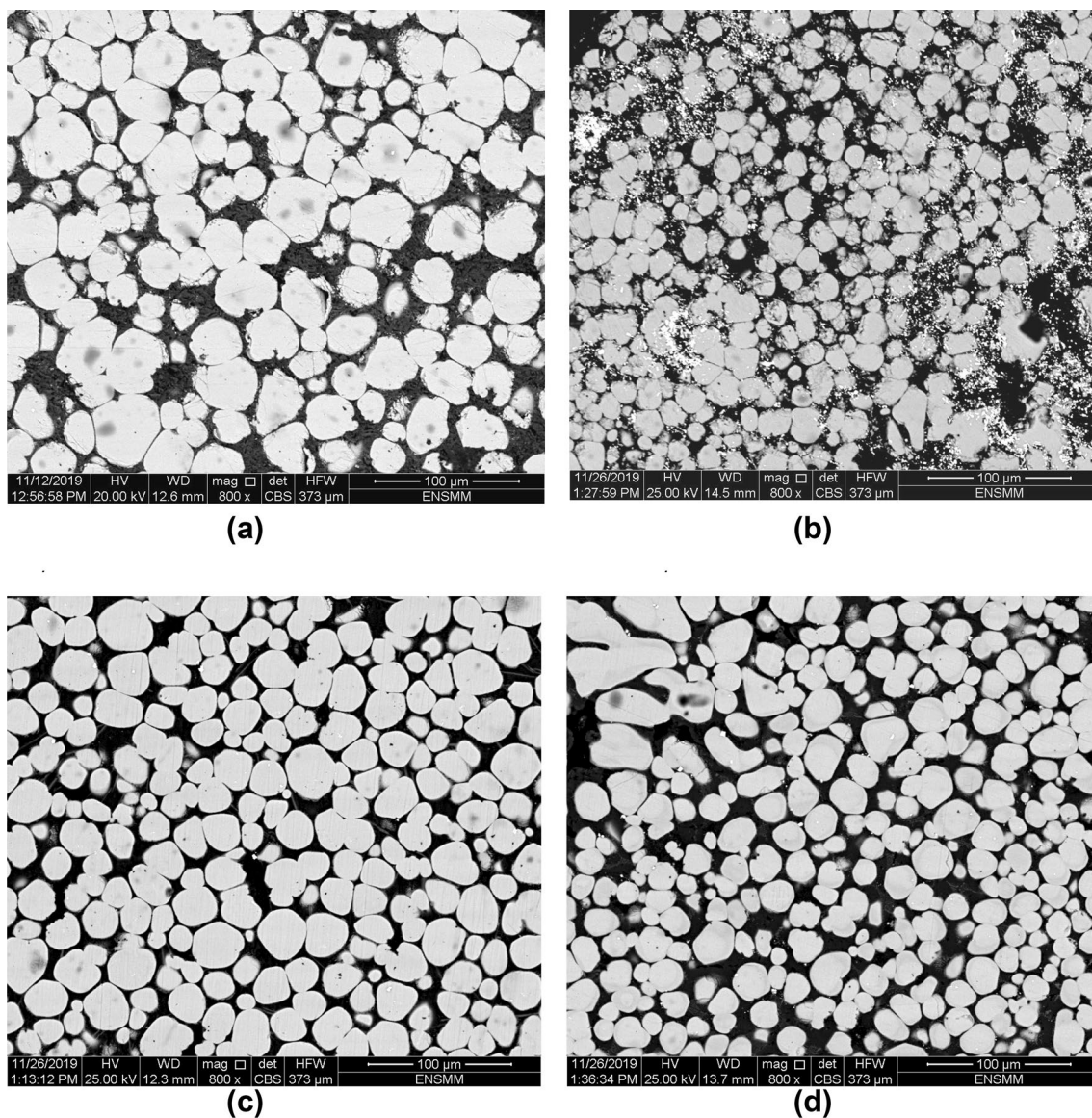


Fig. 3 a–d. BSE images as-cast alloys: (a) Al-40Nb, (b) Al-40Nb-2B, (c) Al-40Nb-2Si, (d) Al-40Nb-2Ti

3.3 Microstructure

Figure 3a–d and 4a–d shows scanning electron microscopy in backscattered electrons (BSE) examinations of the microstructure on all as-cast and heat-treated alloys. Indeed, the structure is primarily composed of two phases: Al solid solution and intermetallic Al_3Nb uniformly disseminated within

the aluminum matrix with an almost cuboidal shape and a volume fraction estimated to be around 80% of the total volume, with an average particle size of 10 to 30 μm . Figure 3b and 4b corresponds to alloy #1 as-cast and heat-treated, respectively, and shows Al_3Nb particles, Figs. 5a–c, covered with flakes of another phase (Fig. 5b) identified as AlB_2 by EDS. This result confirms that of DSC, Fig. 2b. During the

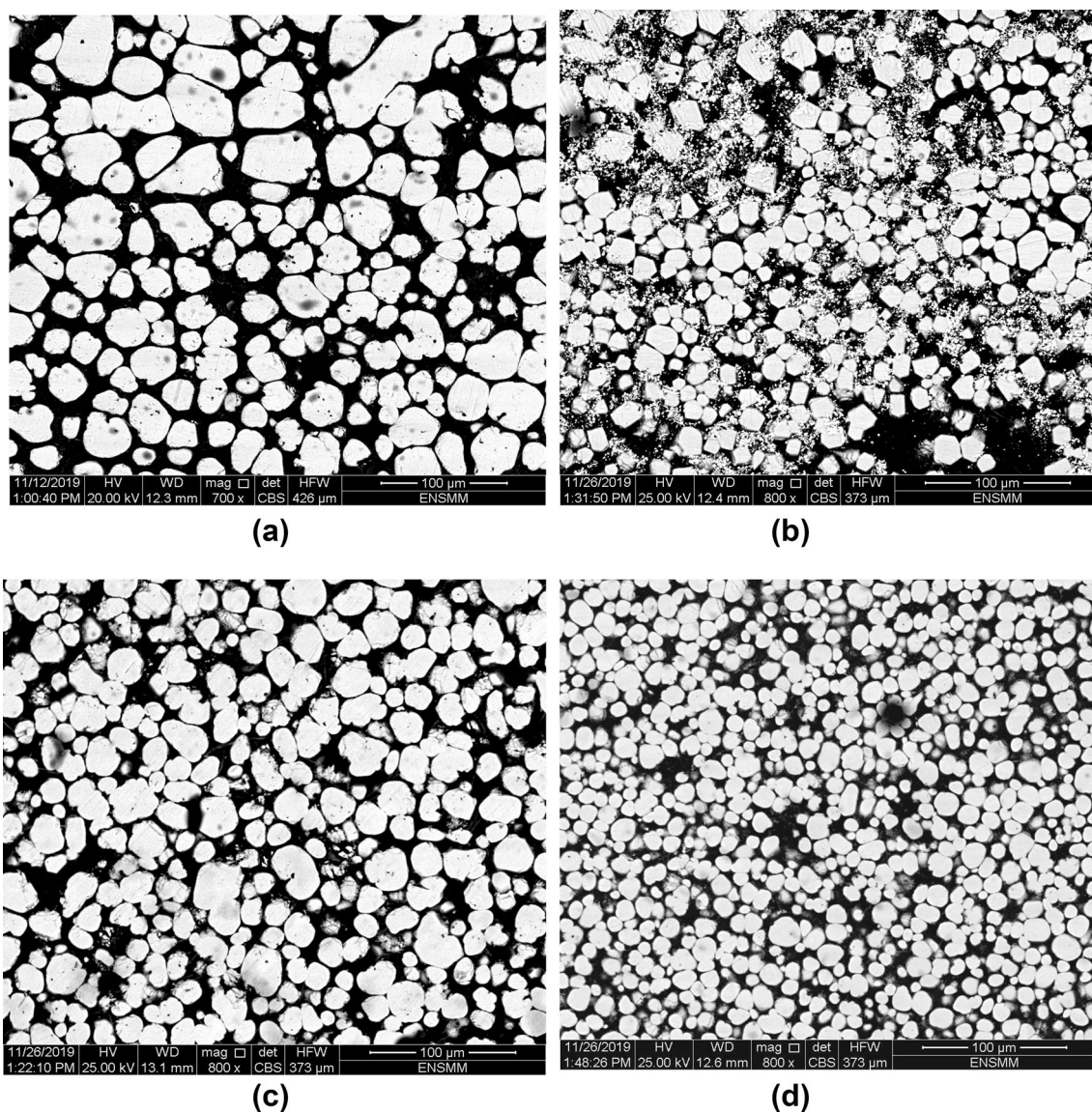


Fig. 4 a–d. BSE images heat-treated alloys (a) Al-40Nb, (b) Al-40Nb-2B, (c) Al-40Nb-2Si, (d) Al-40Nb-2Ti

solidification of liquid aluminum alloys, AlB_2 flakes form [17–20]. Borides have a hexagonal close packed crystal structure (HCP). They can form a fine flake-like structure depending on the cooling rate [8].

3.4 Electrochemical measurements

3.4.1 Potentiodynamic polarization curve

The effect of adding a third element on potentiodynamic polarization curves in Al-40% Nb alloy as cast and heat-treated after immersion for 24 h in 3.5 wt.% NaCl solution is shown in Figs. 6a and b, which is a superposition of the Tafel plot. As can be seen, as-cast and heat-treated alloys

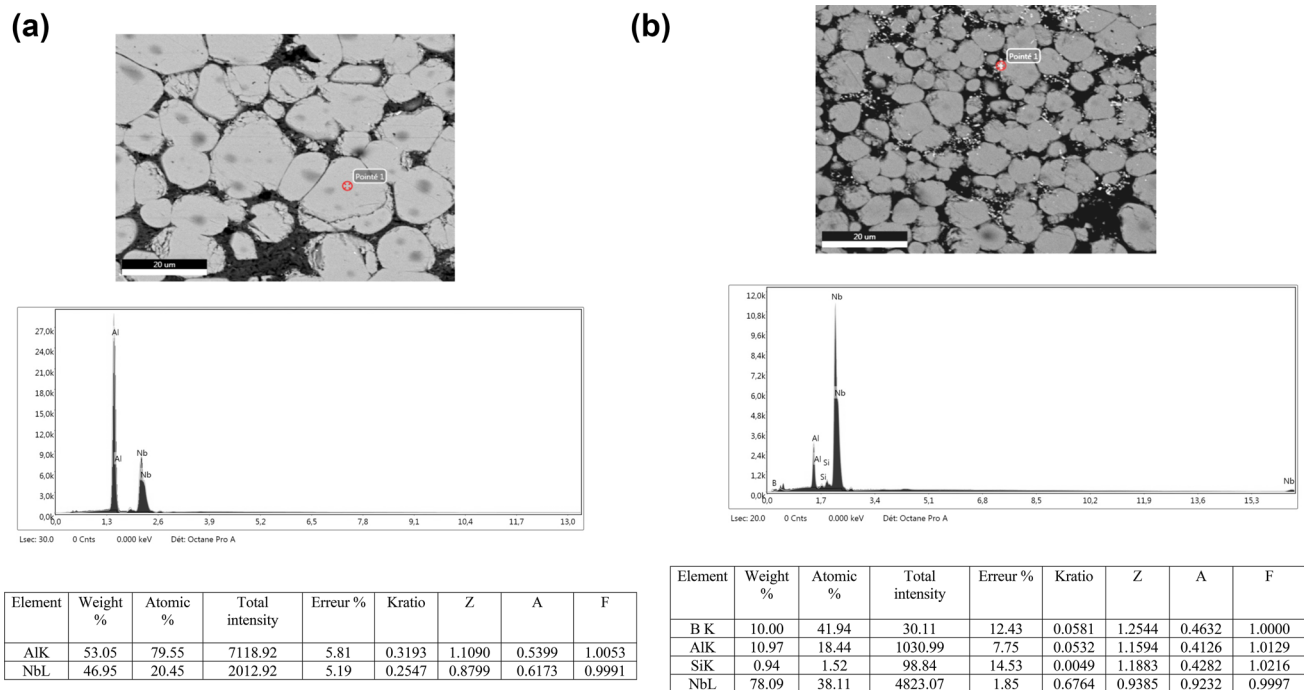


Fig. 5 a–b. EDS analysis from alloy #4 and alloy #1

have different corrosion behavior. The fitted values of β_c , β_a , the corrosion potential (E_{corr}), and the corrosion current density (I_{corr}) of the Al-Nb-X system were obtained from the polarization curves using the Tafel curves extrapolation method and are listed in Tables 2 and 3. The pitting potential of alloys grows with the nature of more elements in the order of #4 as cast < #2 as cast < #3 as cast < #1 as cast, Fig. 7. From this perspective, pitting occurs more quickly in sample #4 as cast because it includes the highest proportion of aluminum. Figure 7 depicts the effect of a 1-h heat treatment at 500 °C, which results in a drop in the potential towards the noble value for all alloys, particularly alloy #3. It should be noted that most commercial alloys have a lower E_{pit} than pure aluminum. Alloying Elements and Their Effects $\text{Mo} > \text{V} > \text{Ni} > \text{Nb} > \text{Cr} > \text{Si} > \text{Ti} > \text{Mn}$ is the order in which the

alloying elements influence the ennobling of the E_{pit} in aluminum binary alloys [49, 50].

The value of corrosion rate, which changes with the type of the elements in order, backs up this conclusion alloy #4 (as-cast) < alloy #2 (as-cast) < alloy #3 (as-cast) < alloy #1 (as-cast) Fig. 8. The difference in microstructure is mostly responsible for this finding. The greatest Rp values are 2.497(k. cm²) and 5.470(k. cm²) for alloy #3 as-cast and alloy #1 heat treated, respectively. The corrosion rates for alloy #1 as-cast and alloy #2 heat-treated are $170.95 \times 10^{-3}(\text{mm. y}^{-1})$ and $144.741 \times 10^{-3}(\text{mm. y}^{-1})$ respectively. Table 4 compares the electrochemical properties of several binary and ternary aluminum alloys reported in the literature, indicating how alloying components affect corrosion behavior. The volume proportion of the second phase,

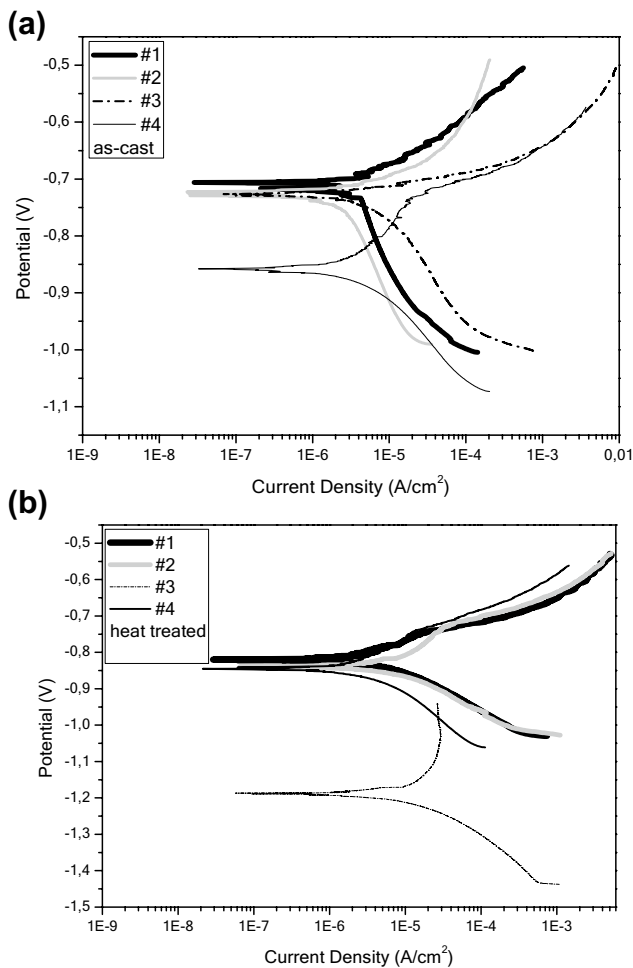


Fig. 6 **a.** Potentiodynamic polarization curves of Al–Nb and Al–Nb–X alloys as cast in 3.5 wt.% NaCl medium at room temperature. **b.** Potentiodynamic polarization curves of Al–Nb and Al–Nb–X heat treated alloys in 3.5 wt.% NaCl medium at room temperature

Table 2 Electrochemical parameters of Al–Nb and Al–Nb–X as-cast with different Nb content 3.5% NaCl solution at room temperature

Alloy state	Potential (VSCE)	Current density ($\mu\text{A}\cdot\text{cm}^{-2}$)	Cathodic beta (VSCE)	Anodic beta (VSCE)	$R_p(\text{k}\Omega\cdot\text{cm}^2)$	$C_R \times 10^{-3} (\text{mm}\cdot\text{y}^{-1})$
As-cast						
Alloy #1	−0.710	17.717	0.317	0.066	1.344	170.95
Alloy #2	−0.726	4.397	0.129	0.029	2.387	44.42
Alloy #3	−0.725	7.447	0.295	0.050	2.497	74.22
Alloy #4	−0.859	3.82	0.101	0.177	9.93	38.1

Table 3 Electrochemical parameters of Al–Nb and Al–Nb–X heat treated with different Nb content 3.5% NaCl solution at room temperature

Alloy state	Potential (V_{SCE})	Current density ($\mu\text{A}\cdot\text{cm}^{-2}$)	Cathodic beta (V_{SCE})	Anodic beta (V_{SCE})	$R_p (\text{k}\Omega\cdot\text{cm}^2)$	$C_R \times 10^{-3} (\text{mm}\cdot\text{y}^{-1})$
Heat treated						
Alloy #1	−0.810	2.754	0.082	0.060	5.470	26.57
Alloy #2	−1.192	14.325	0.122	0.362	2.760	144.741
Alloy #3	−0.834	6.242	0.100	0.091	3.326	62.211
Alloy #4	−0.743	5.00	0.239	0.044	3.25	49.9

as well as its distribution in the matrix, influence corrosion resistance. As a result, the alloy's hardness is critical, and it increases in lockstep with the corrosion potential [49]. The hardness of the binary Al–40% Nb alloy, for example, is around 423.5Hv, rising to 490.85Hv for Al–40% Nb–2%Ti, 494.16Hv for Al–40% Nb–2% B, and 456.27 Hv for Al–40% Nb–2% Si.

3.4.2 Electrochemical impedance spectroscopy (EIS)

Figure 9a–b shows Nyquist plots of as-cast and heat-treated Al–Nb alloys assessed in a 3.5 wt.% NaCl solution at room temperature. A semicircle arcs diagram is commonly regarded as a charge transfer mechanism on an inhomogeneous surface [53, 54]. By assuming an electric equivalent circuit (ECC) for the interface between electronic (electrode) and ionic conducting (electrolyte) materials, semicircle behavior can be understood. EC-Lab® V10.37 is used to fit EIS data, as well as a complicated equivalent circuit model of samples with distinct addition elements (B, Ti, Si) as-cast alloy #1, as-cast alloy #2, as-cast alloy #3, and binary as-cast (Al–40% Nb). Figure 10 shows alloy # 4, which is made up of resistance (R_s) in series with (Z_{CPE1}) in parallel arrangement with (R_1) and (Z_{CPE2}) in parallel arrangement with (R_2), where R_s is the ohmic resistance of the electrolyte between the working electrode (W_E) and reference electrode (R_E). In addition, Z_{CPE1} denotes the oxide layer's capacitance, whereas R_1 denotes the passive layer's polarization resistance. The Z_{CPE2} constant phase element is also important to consider because of the double layer capacitance, and R_2 is the charge transfer resistance. $Z_{\text{CPE}} = 1/(Q(i\omega)^n)$ $i = (-1)^{1/2}$, ω is the angular frequency, $\omega = 2\pi f$ and f is the frequency, $n = 0$ corresponds to a pure resistor, $n = 1$ to a

Fig. 7 Pitting potential (E_{pit}) variation versus third element (As-cast and heat treated)

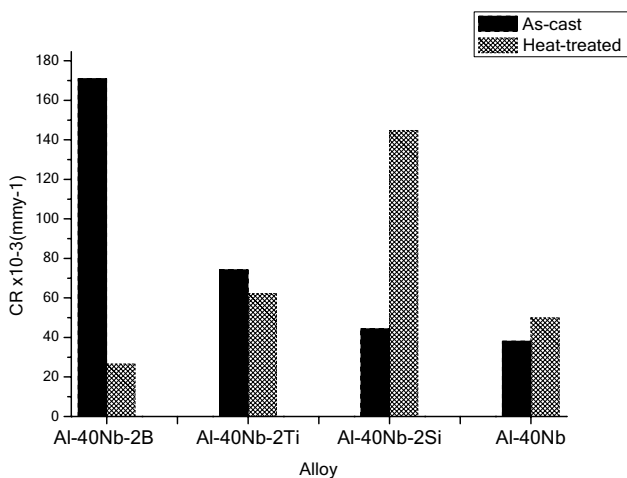
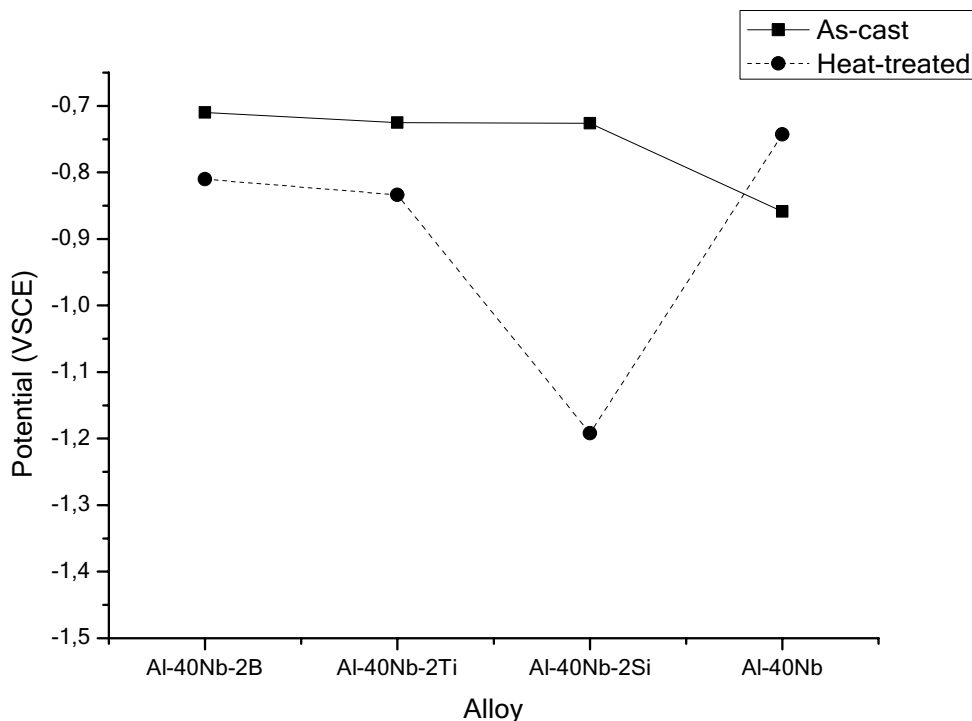


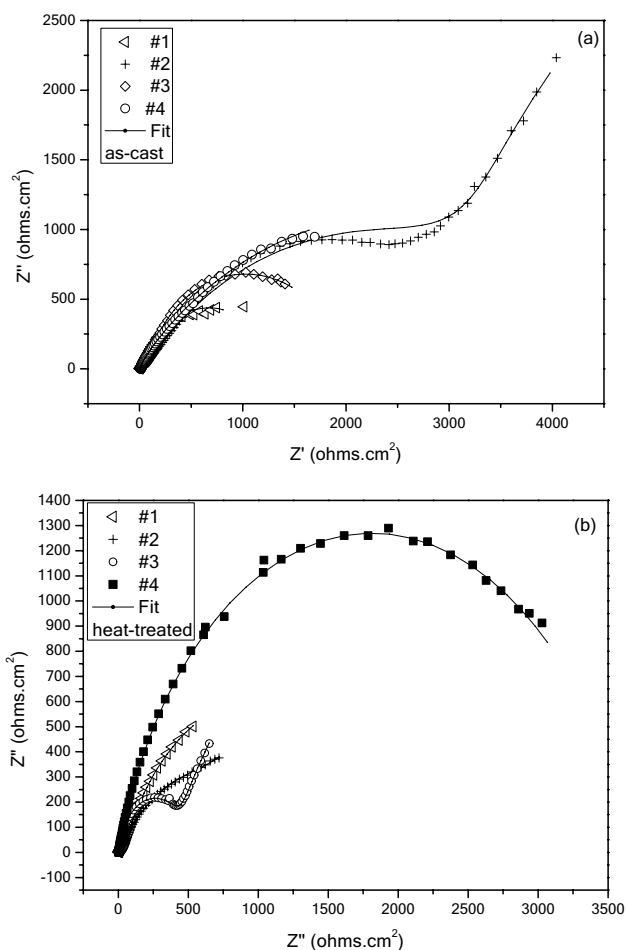
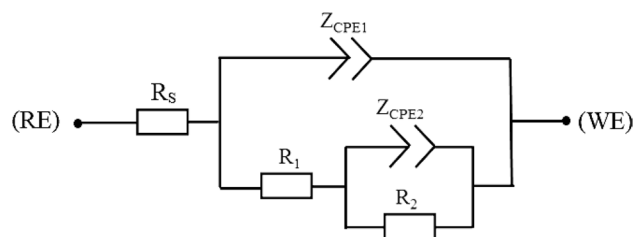
Fig. 8 Corrosion rate variation versus nature of addition element (As-cast and heat-treated)

pure capacitor, and $n=0.5$ to a Warburg type impedance [55].

Porosity and roughness have been linked to changes in n value [56]. The corrosion resistance is proportional to the diameter of the Nyquist semicircle. It's worth noting that the best electrochemical corrosion behavior corresponds to the largest semicircle arc. Higher R_{ct} values indicate the creation of a persistent oxide layer on the surface, which significantly improves the alloy's corrosion resistance. Two dominant processes may be envisaged occurring in tandem, according to Nyquist plots: one capacitive behavior of charge separation at interface and the other resistive behavior of electron transfer process. The combination of these two processes produces a capacitive semicircle response on a Nyquist plot, from which the Nyquist data for alloy #2 as cast (Fig. 11a) exhibit arc-like behavior over the frequency

Table 4 Electrochemical features of some Al base alloys

Alloy system	i_{corr} ($\mu\text{A} \cdot \text{cm}^{-2}$)	E_{corr} (V_{SCE}) mV	β_a (mV/dec)	β_c (mV/dec)	Epit (V_{SCE})	Rp ($k\Omega \text{cm}^2$)	CR (mm/year)	Refs
Al-9%Si	0.98	-722	-	-	-	-	-	[36]
Al-7% Si As-cast	-	-600	-	-	-	-	0.0216	[33]
Al-7% Si Heat-treated	-	-925	-	-	-	-	0.002	[33]
Al-10%Cu-5%Ti	8.2	-1.1	255	145	-	4.90	0.09	[40]
Al-5%Ti	-	-	-	-	-303	-	-	[49]
Al-5%Mo	-	-	-	-	-46	-	-	[49]
Al-5%V	-	-	-	-	-120	-	-	[49]
Al-5%Si	-	-	-	-	-202	-	-	[49]
Al-5%Nb	-	-	-	-	-144	-	-	[49]
Al-40%Nb As-cast	0.38	-859	177	101	-	9.93	0.00381	Present work
Al-40%Nb Heat-treated	0.05	-743	44	239	-	3.25	0.00499	Present work
Al-24%Co	0.13	-706	-	-	-	-	-	[51]
Al-15%Co-2%Ti	0.04	-490	-	-	-	-	-	[52]

**Fig. 9** a–b Nyquist plots of Al-Nb alloys as-cast and heat-treated**Fig. 10** Equivalent circuit model of samples with different addition elements (B, Ti, Si)

range investigated and the diameter of the arc is larger than of the other samples and is associated with lower corrosion rate [57, 58], for heat-treated alloys it is alloy #4 which shows the best impedance parameter obtained after the fit. The changes on the surface of the sample during the EIS experiment were seen using the Bode plot generated from the EIS data.

Figure 11a shows that the impedance value of alloy #2 as-cast is the highest over the entire frequency range, while alloy #4 has the lowest impedance in both the medium and high-frequency ranges. Otherwise, heat-treated alloys #3, #2, and #4 have the highest impedance value in the low-frequency range, while alloys #4, #1, #2, and #3 have the highest impedance value in the high-frequency range. The alloys #2, #3, #1, and #4 have the highest impedance in the medium-frequency band. The Bode-phase plots reveal two-time constants, as shown in Fig. 11b, which reflects a highly capacitive behavior typical of passive materials [59]. Two-time constants result from a heterogeneous surface induced by defects and/or element segregation [60]. Low-frequency phase angles approaching 60° for as-cast #4 and heat-treated

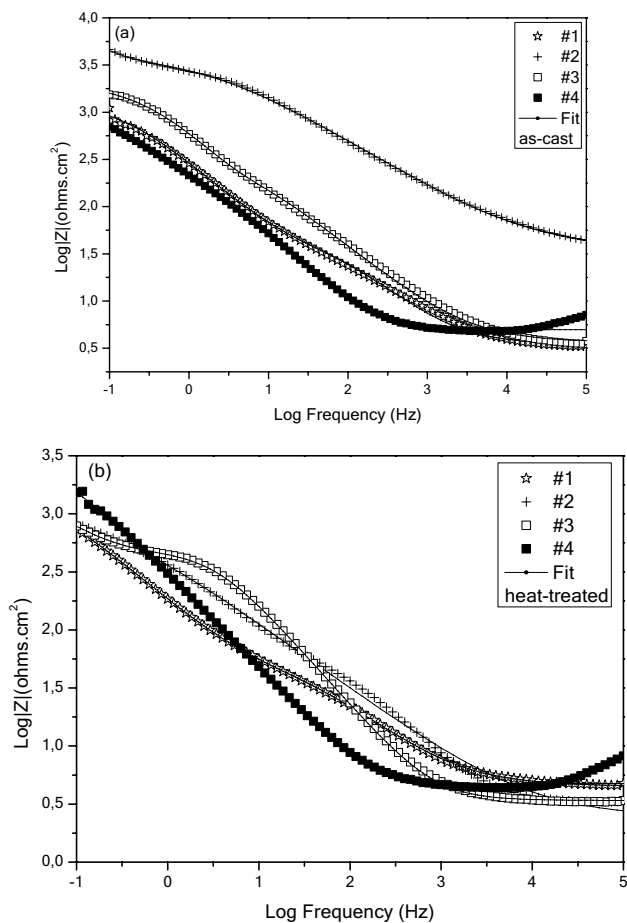


Fig. 11 a–b. Bode plots of Al-Nb alloys as-cast and heat-treated

#3 alloys, and phase angles approaching 70° for heat-treated alloy #4 and alloy #3 alloys, indicating capacitive behavior (Figure 12a and b). In the medium-frequency range, alloy 3# [61] had the largest phase angle, which was close to 60° at high-intermediate frequencies. The creation of the surface oxide layer corresponds to the first peak in the middle frequency for all alloys.

4 Conclusion

The nature of the additional element (such as boron, silicon, or titanium) added to the binary alloy Al-40% Nb rapidly solidified after melting under magnetic induction has an impact not only on the microstructure but also on the electrochemical properties after immersion in saline solution, as shown in this study.

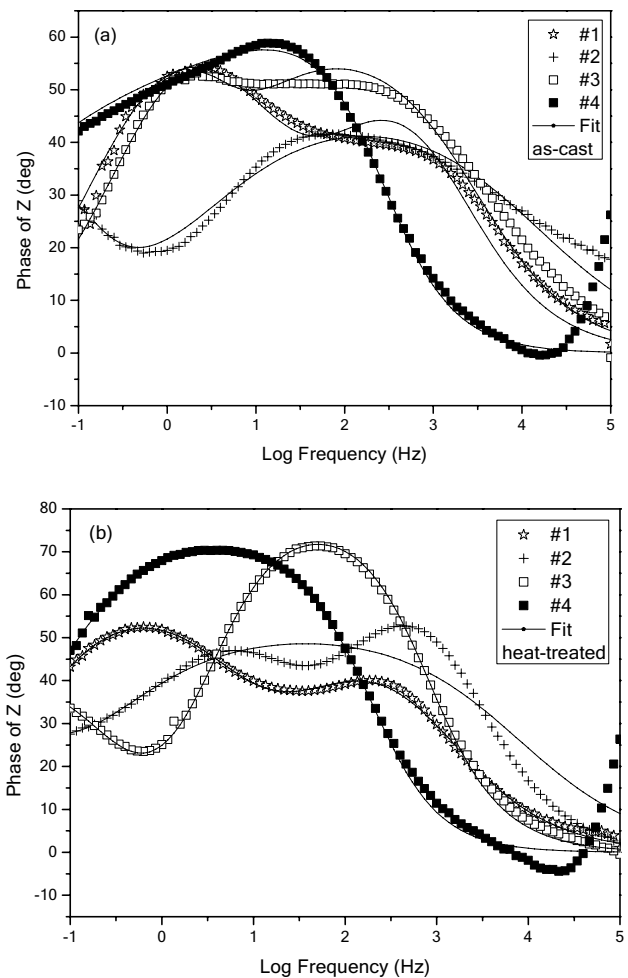


Fig. 12 a–b. Phase plots of Al-Nb alloys as-cast and heat-treated

In the raw condition, the three components considerably improve the binary alloy's corrosion and strengthening characteristics.

The pitting potential of alloys increases with the nature of additional elements in the order of #4 as-cast < #2 as-cast < #3 as-cast < #1 as-cast, according to the findings.

The corrosion rate changes with the nature of the elements in the following order: alloy #4 as-cast < alloy #2 as-cast < alloy #3 as-cast < alloy #1 as-cast. However, after 1 h of heat treatment at 500°C , the ternary alloy containing silicon has the lowest corrosion potential when compared to the two other alloys containing boron and titanium, respectively, as well as the alloy without addition, which sees its potential increase solely due to temperature action.

Acknowledgements The authors are very grateful to the DGRSDT for financial assistance and to researchers at the ENSMM Annaba for SEM observations.

Declarations

Conflict of interest The authors declare that they have no conflict of interest.

References

- Audebert F, Galano M, Saporiti F (2014) The use of Nb in rapid solidified Al alloys and composites. *J. Alloys Compounds* 615:S621–S626. <https://doi.org/10.1016/j.jallcom.2013.12.129>
- Schwarz H-G, Briem S, Zapp P (2001) Future carbon dioxide emissions in the global material flow of primary aluminium. *Energy* 26(8):775–795. [https://doi.org/10.1016/S0360-5442\(01\)00032-9](https://doi.org/10.1016/S0360-5442(01)00032-9)
- Hirsch J (2011) Aluminium in innovative light-weight car design. *Mater Trans* 52(5):818–824. <https://doi.org/10.2320/matertrans.L-MZ201132>
- Toros S, Ozturk F, Kacar I (2008) Review of warm forming of aluminum–magnesium alloys. *J Mater. Process Technol* 207(1–3):1–12. <https://doi.org/10.1016/j.jmatprotec.2008.03.057>
- Rambabu P, Prasad NE, Kutumbarao VV, Wanhill RJH (2017) Aluminium alloys for aerospace applications. In: Prasad NE, Wanhill RJH (eds) *Aerospace materials and material technologies*. Springer, Singapore, pp 29–52
- K. A. Yasakau, M. L. Zheludkevich, M. G. S. Ferreira, Role of intermetallics in corrosion of aluminum alloys. In *Smart corrosion protection, in Intermetallic Matrix Composites*, Elsevier, 2018, p. 425–462.
- Ujah CO, Popoola API, Popoola OM, Aigbodion VS (2018) Electrical conductivity, mechanical strength and corrosion characteristics of spark plasma sintered Al–Nb nanocomposite. *Int J Adv Manuf Technol*. <https://doi.org/10.1007/s00170-018-3128-x>
- Shibli SMA, Jabeera B, Manu R (2007) Development of high performance aluminium alloy sacrificial anodes reinforced with metal oxides. *Mater Lett* 61(14–15):3000–3004. <https://doi.org/10.1016/j.matlet.2006.10.062>
- Pramod SL, Bakshi SR, Murty BS (2015) Aluminum-based cast in situ composites: a review. *J Mater Eng Perform* 24(6):2185–2207. <https://doi.org/10.1007/s11665-015-1424-2>
- Di Franco F, Santamaria M, Di Quarto F, La Mantia F, de Sá AI, Rangel CM (2013) Dielectric properties of Al–Nb amorphous mixed oxides. *ECS J State Science Technol* 2(11):205–210. <https://doi.org/10.1149/2.012311jss>
- Ghandvar H, Idris MH, Asma T, Bakar A, Nafari A, Ahmad N (2020) Microstructural characterization, solidification characteristics and tensile properties of Al 15%Mg2Si–x(Gd–Sb) in-situ composite. *J Mater Res Technol* 9(3):3272–3291
- Abboud J, Mazumder J (2020) Developing of nano sized fibrous eutectic silicon in hypereutectic Al–Si alloy by laser remelting. *Sci Rep* 10:12090. <https://doi.org/10.1038/s41598-020-69072-1>
- Saidman SB, Garcia SG, Bessone JB (1995) Electrochemical behaviour of Al–In alloys in chloride solutions. *J Appl Electrochem*. <https://doi.org/10.1007/BF00262964>
- D. R. Salinas, Influence of alloying elements and microstructure on aluminium sacrificial anode performance: case of Al±Zn, p. 9.
- Shayeb HAE (2001) Effect of gallium ions on the electrochemical behaviour of Al, Al±Sn, Al±Zn and Al±Zn±Sn alloys in chloride solutions. *Corr Sci* 43(3):643–654
- Gudić S, Smoljko I, Kliškić M (2010) Electrochemical behaviour of aluminium alloys containing indium and tin in NaCl solution. *Mater Chem Phys* 121(3):561–566. <https://doi.org/10.1016/j.matchemphys.2010.02.040>
- Mostaan H, Karimzadeh F, Abbasi MH (2012) Thermodynamic analysis of nanocrystalline and amorphous phase formation in Nb–Al system during mechanical alloying. *Powder Metallurgy* 55(2):142–147. <https://doi.org/10.1179/1743290111Y.000000018>
- Gauthier V, Bernard F, Gaffet E, Vrel D, Gailhanou M, Larpin JP (2002) Investigations of the formation mechanism of nanostructured NbAl3 via MASHS reaction. *Intermetallics* 10(4):377–389. [https://doi.org/10.1016/S0966-9795\(02\)00010-9](https://doi.org/10.1016/S0966-9795(02)00010-9)
- Almeida A, Petrov P, Nogueira I, Vilar R (2001) Structure and properties of Al–Nb alloys produced by laser surface alloying. *Mater Sci Eng A* 303(1–2):273–280. [https://doi.org/10.1016/S0921-5093\(00\)01838-4](https://doi.org/10.1016/S0921-5093(00)01838-4)
- Mareci D, Popa IM, Ungureanu G, Aelenei D, MirzaRosca JC (2006) Electrochemical response of aluminum in contact with beer. *Sci Study Res-Chem Chem Eng Biotechnol Food Ind* 7(4):769–778
- Rana RS, Purohit R, Das S (2012) Reviews on the influences of alloying elements on the microstructure and mechanical properties of aluminum alloys and aluminum. *Alloy Composites* 2(6):8
- Guzowski MM, Sigworth GK, Sentner DA (1987) The role of boron in the grain. *MTA* 18(4):603–619. <https://doi.org/10.1007/BF02649476>
- Chen Y, Pan Y, Lu T, Tao S, Wu J (2014) Effects of combinative addition of lanthanum and boron on grain refinement of Al–Si casting alloys. *Mater Design* 64:423–426. <https://doi.org/10.1016/j.matdes.2014.07.068>
- Yuying W, Xiangfa L, Xiufang B (2007) Effect of boron on the microstructure of near-eutectic Al–Si alloys. *Mater Characterization* 58(2):205–209. <https://doi.org/10.1016/j.matchar.2006.04.009>
- Sarkar R, Ghosal P, Muraleedharan K, Nandy TK, Ray KK (2011) Effect of boron and carbon addition on microstructure and mechanical properties of Ti–15–3 alloy. *Mater Sci Eng A* 528(13–14):4819–4829. <https://doi.org/10.1016/j.msea.2011.03.014>
- Hernandez-Rodriguez M, Laverde-Cataño D, Lozano D, Martinez-Cazares G, Bedolla-Gil Y (2019) Influence of boron addition on the microstructure and the corrosion resistance of CoCrMo alloy. *Metals* 9(3):307. <https://doi.org/10.3390/met9030307>
- Wang M, Hu K, Liu G, Liu X (2020) Synchronous improvement of electrical and mechanical performance of A356 alloy reinforced by boron coupling nano-AlNp. *J Alloys Compounds* 814:152217. <https://doi.org/10.1016/j.jallcom.2019.152217>
- Cui X, Wu Y, Zhang G, Liu Y, Liu X (2017) Study on the improvement of electrical conductivity and mechanical properties of low alloying electrical aluminum alloys. *Composites B Eng* 110:381–387. <https://doi.org/10.1016/j.compositesb.2016.11.042>
- Cui X, Wu Y, Liu X, Zhao Q, Zhang G (2015) Effects of grain refinement and boron treatment on electrical conductivity and mechanical properties of AA1070 aluminum. *Mater Design* 86:397–403. <https://doi.org/10.1016/j.matdes.2015.06.149>
- Zhu J, Kamiya A, Yamada T, Shi W, Naganuma K (2003) Influence of boron addition on microstructure and mechanical properties of dental cast titanium alloys. *Mater Sci Eng A* 339(1–2):53–62. [https://doi.org/10.1016/S0921-5093\(02\)00102-8](https://doi.org/10.1016/S0921-5093(02)00102-8)
- Yan BC, Zhang J, Lou LH (2008) Effect of boron additions on the microstructure and transverse properties of a directionally solidified superalloy. *Mater Sci Eng A* 474(1–2):39–47. <https://doi.org/10.1016/j.msea.2007.05.082>

32. Baetzner C, Beuers J, Hoch M, Korniyenko K (2009) Aluminum—Niobium—Silicon. *LandoltBörnstein*. https://doi.org/10.1007/978-3-540-88053-0_12
33. El-Aziz KA, Saber D, Sallam HE-DM (2015) Wear and corrosion behavior of Al–Si matrix composite reinforced with alumina. *J Bio TriboCorros* 1(1):5. <https://doi.org/10.1007/s40735-014-0005-5>
34. Osório WR, Goulart PR, Garcia A (2008) Effect of silicon content on microstructure and electrochemical behavior of hypoeutectic Al–Si alloys. *Mater Lett* 62(3):365–369. <https://doi.org/10.1016/j.matlet.2007.05.051>
35. Bandil K et al (2019) Microstructural, mechanical and corrosion behaviour of Al–Si alloy reinforced with SiC metal matrix composite. *J Composite Mater* 53(28–30):4215–4223. <https://doi.org/10.1177/0021998319856679>
36. Osório WR, Cheung N, Spinelli JE, Goulart PR, Garcia A (2007) The effects of a eutectic modifier on microstructure and surface corrosion behavior of Al–Si hypoeutectic alloys. *J Solid State Electrochem* 11(10):1421–1427. <https://doi.org/10.1007/s10008-007-0300-x>
37. Revilla RI, De Graeve I (2018) Influence of Si content on the microstructure and corrosion behavior of additive manufactured Al–Si alloys. *J. Electrochem. Soc.* 165(13):C926–C932. <https://doi.org/10.1149/2.0101814jes>
38. Kumar V, Mehdi H, Kumar A (2015) Effect of silicon content on the mechanical properties of aluminum. *Alloy* 02(04):6
39. Sasikumar Y, Indira K, Rajendran N (2019) Surface modification methods for titanium and its alloys and their corrosion behavior in biological environment: a review. *J Bio TriboCorros* 5(2):36. <https://doi.org/10.1007/s40735-019-0229-5>
40. Sherif E-SM, Ammar HR, Khalil KA (2014) Effects of copper and titanium on the corrosion behavior of newly fabricated nanocrystalline aluminum in natural seawater. *Appl Surf Sci* 301:142–148. <https://doi.org/10.1016/j.apsusc.2014.02.019>
41. Yasakau KA, Zheludkevich ML, Ferreira MGS (2018) Role of intermetallics in corrosion of aluminum alloys. In: Mitra R (ed) *Smart corrosion protection*. Woodhead Publishing, Intermetallic Matrix Composites, pp 425–462
42. Knipling KE, Dunand DC, Seidman DN (2006) Criteria for developing castable, creep-resistant aluminum-based alloys—a review. *Z Metallkd* 97(3):246
43. Witusiewicz VT, Bondar AA, Hecht U, Rex S, Velikanova TY (2008) The Al–B–Nb–Ti system: III. Thermodynamic re-evaluation of the constituent binary system Al–Ti. *J. Alloys Compd.* 465:64
44. Fan QH, Zhao YM, Huang J, Ouyang LS, Kuang Q (2012) Large-scale synthesis of aluminum diboride nanowires by Ni(NO₃)₂ catalyst. *J Cryst Growth* 346:75–78
45. Djurdjević MB, Manasijević S, Odanović Z, Dolić N (2013) Calculation of liquidus temperature for aluminum and magnesium alloys applying method of equivalency. *Adv Mater Sci Eng* 2013:1–8
46. Wang S, Xiazhang MF, Wang LJ, Su X (2018) *J Mater Process Technol* 255:105–109
47. Prach O, Trudonoshyn O, Puchnin M (2017) Effects of chemical composition on mechanical properties of Al–Mg–Si–Mn based alloys. *Mater Eng—Materiálové inžinierstvo* 24:11–20
48. Mondolfo LF (1976) *Aluminum alloys: structure and properties*. Butterworths, London, pp 312–53
49. Esquivel J, Murdoch HA, Darling KA, Gupta RK (2018) Excellent corrosion resistance and hardness in Al alloys by extended solid solubility and nanocrystalline structure. *Mater Res Lett* 6(1):79–83. <https://doi.org/10.1080/21663831.2017.1396262>
50. Pride ST, Scully JR, Hudson JL (1994) Metastable pitting of aluminum and criteria for the transition to stable pit growth. *J Electrochem Soc* 141:3028–3040
51. Palcut M, Priputen P, Šalgó K, Janovec J (2015) Phase constitution and corrosion resistance of Al–Co alloys. *Mater Chem Phys* 166:95–104
52. Debili MY, Sassane N, Boukhris N (2017) Structure and corrosion behavior of Al–Co–Ti alloy system. *Anti Corros Methods Mater* 64:443–451
53. Shi YZ, Yang B, Xie X, Brechtl J, Dahmen KA, Liaw PK (2017) Corrosion of Al_xCoCrFeNi high-entropy alloys: Al content and potential scan-rate dependent pitting behavior. *Corros Sci* 119:33
54. Singh D, Dhayal V, Agarwal DC (2019) *Surf Eng Appl Electrochem* 55(4):436–442
55. A. Toloei, V. Stoilov, D. Northwood. Proceedings of the ASME 2013 International Mechanical Engineering Congress & Exposition IMECE 2013 November 13–21, 2013, San Diego, California, USA.
56. Chen Y, Jepson WP (1999) EIS measurement for corrosion monitoring under multiphase flow conditions. *Electrochim Acta* 44(24):4453–4464
57. Prakashaiah, B. G., *Corros Sci* (2018). <https://doi.org/10.1016/j.corsci.2018.03.021>.
58. Arthanari S, Jang JC, Shin KS (2019) *J Alloys Compd* 783:494–502
59. Seikh AH, Baig M, Ammar HR, Alam MA (2016) The influence of transition metals addition on the corrosion resistance of nanocrystalline Al alloys produced by mechanical alloying. *Metals* 6:140
60. Morquech CPC et al (2012) *Int. J. Electrochem. Sci.* 7:1125–1133
61. Liyana NK, Fazal MA, Haseeb ASMA (2018) Polarization and EIS studies to evaluate the effect of aluminum concentration on the corrosion behavior of SAC105 solder alloy. *Mater Sci-Poland* 35(4):694–701

Publisher's Note Springer Nature remains neutral with regard to jurisdictional claims in published maps and institutional affiliations.